The intersection of inflammation and DNA damage as a novel axis underlying the pathogenesis of autism spectrum disorders

Megha Jhanji [1,2], Colleen L. Krall [1,2], Alexis Guevara [1,2], Brian Yoon [1,2], Mathew Sajish [3], Luigi Boccuto [4,5], and Sofia B. Lizarraga [1,2&]

[1] Department of Molecular Biology, Cell Biology and Biochemistry, Brown University, Providence, RI
[2] Center for Translational Neuroscience, Carney Brain Institute, Brown University, Providence, RI
[3] Department of Drug Discovery and Biomedical Sciences, College of Pharmacy, University of South Carolina, Columbia, SC
[4] JC Self Research Institute, Greenwood Genetic Center, Greenwood, SC
[5] School of Nursing, College of Behavioral, Social, and Health Sciences, Clemson University, Clemson, SC

[&] Corresponding author: sofia_lizarraga@brown.edu

Running title: Inflammatory pathways induce DNA damage response in human neurons

ABSTRACT

Autism spectrum disorders (ASD) affects 1 in 36 children and is characterized by repetitive behaviors and difficulties in social interactions and social communication. The etiology of ASD is extremely heterogeneous, with a large number of ASD cases that are of unknown or complex etiology, which suggests the potential contribution of epigenetic risk factors. In particular, epidemiological and animal model studies suggest that inflammation during pregnancy could lead to an increased risk of ASD in the offspring. However, the molecular mechanisms that contribute to ASD pathogenesis in relation to maternal inflammation during pregnancy in humans are underexplored. Several pro-inflammatory cytokines have been associated with increased autistic-like behaviors in animal models of maternal immune activation, including IL-17A. Using a combination of ASD patient lymphocytes and stem cell-derived human neurons exposed to IL-17A we discovered a shared molecular signature that highlights a metabolic and translational node that could lead to altered neuronal excitability. Further, our work on human neurons brings forward the possibility that defects in the DNA damage response could be underlying the effect of IL-17A on human excitatory neurons, linking exacerbated unrepaired DNA damage to the pathogenicity of maternal inflammation in connection to ASD.

Key words: *ASD, DNA damage, IL-17A, MIA, translation, stem cell derived-neurons*

INTRODUCTION

Large epidemiological studies suggest that maternal infection during pregnancy could be a major environmental risk factor for autism spectrum disorders (ASD) (Lee *et al*, 2015; Lydholm *et al*, 2019). Severe viral infections during pregnancy are associated with a one-third increase in ASD risk in offspring (Lee *et al.*, 2015). For example, an analysis of 96,000 Danish children showed that risk for ASD doubled in response to severe maternal influenza infection (Atladottir *et al*, 2012). Evidence from clinical and postmortem studies suggests an emergent immune signature associated with ASD. Blood samples from individuals with ASD showed higher gene expression of pro-inflammatory genes such as TNF-α, IL-6, and IL-17 compared to controls (Eftekharian *et al*, 2018). Similarly, transcriptome analyses of postmortem brain tissues identified an overrepresentation of genes involved in immune regulation in ASD brains compared to unaffected individuals (Sciara *et al*, 2020; Voineagu *et al*, 2011). Work from animal models of maternal immune activation (MIA) suggests that a major mechanism underlying the effect of MIA during mammalian brain development is the IL-6/IL-17A immunoregulatory axis. MIA leads to elevated levels of IL-6, driving the differentiation of Th0 cells into Th-17 cells in the mother (Smith *et al*, 2007). These activated Th17 cells produce IL-17A (Kimura & Kishimoto, 2010), which can cross the placental barrier and disrupt fetal brain development. The direct effect of IL-17A in the developing cerebral cortex was shown in animal models; for example, in-utero injection of IL-17A into the embryonic mouse cortices at day 14.5 (E14.5), led to anatomical and behavioral phenotypes that resemble those associated with MIA (Choi *et al*, 2016). However, mechanistic studies on the role of IL-17A on cortical human neurons and how that might intersect with underlying mechanisms are lacking.

Transcriptome studies of rat fetal brains exposed to MIA during a developmental stage equivalent to the human gestational third trimester showed upregulation of pathways implicated in translation and DNA damage (Lombardo *et al*, 2018). In contrast, treatment of human forebrain organoids with activated IL-6 showed downregulation of genes implicated in translation (Sarieva *et al*, 2023) and implicated a primary effect on neuronal progenitor cells, suggesting a species and cell type-specific response to inflammatory signals in the developing brain. Emerging evidence highlights the therapeutic potential of resveratrol (RSV), a polyphenolic compound with anti-inflammatory and antioxidant properties, in counteracting neuroinflammation and oxidative stress, which are prominent features in ASD models. RSV treatment in animal studies has shown promise in alleviating ASD-like behaviors such as social deficits and repetitive behaviors (Bakheet *et al*, 2016; Bambini-Junior *et al*, 2014; Bhandari & Kuhad, 2017; Fontes-Dutra *et al*, 2018; Xie *et al*, 2018). However, recent findings suggest that RSV's biological effects may differ between its *cis*- and *trans*-isomers, which have distinct mechanisms of action. For instance, these isomers differentially regulate the nuclear

translocation and activity of tyrosyl-tRNA synthetase (TyrRS), a key enzyme involved in DNA repair and stress response (Cao *et al*, 2017; Jhanji *et al*, 2022). These differences could have significant implications for the therapeutic application of RSV in ASD, underscoring the need for isomer-specific studies.

Additionally, clinical evidence suggests that innate immune dysfunction in individuals with ASD may exacerbate behavioral symptoms (Hughes *et al*, 2023). This highlights the potential for therapeutic interventions targeting immune and oxidative stress pathways to extend benefits beyond the prenatal period. However, the extent to which there are common mechanisms altered by inflammation at fetal and postnatal stages in humans in relation to ASD pathogenesis is underexplored. Here, we use IL-17A as well as anti- and pro-inflammatory *cis* and *trans*-resveratrol (*cis*-RSV and *trans*-RSV) to dissect their effect on maturing human neurons mechanistically. We find that exposure to inflammatory signals impairs neurite outgrowth and decreases neuronal activity in stem cell-derived excitatory neurons. These cellular phenotypes correlate with alteration on key downstream signaling pathways, including (STAT3, MAPK, and NF-κB), as well as increased unrepaired DNA damage, which elicits the activation of the innate immune cGAS pathway (Liu *et al*, 2018) and leads to increased nuclear translocation of TyrRS where it activates DNA repair mechanisms (Cao *et al.*, 2017). Additional transcriptomic and WGCNA analysis on stem cell-derived human neurons showed that inflammation leads to functional enrichment primarily on metabolic and translation pathways. Finally, we find that the key molecular signatures identified in stem cell-derived human neurons transcend cell types and genetic background as analysis of lymphocytes obtained from ASD individuals showed similar transcriptome changes.

RESULTS

IL-17A impairs neuronal morphogenesis and activity, with exacerbation by *trans*-RSV

ASD is a disorder of neuronal connectivity, and the proper development of neuronal connections requires precise regulation of neuronal arborization and synaptic function. To explore the impact of inflammatory signaling on human neurons, we used human embryonic stem cell (hESC) line H9 (Thomson *et al*, 1998) and differentiated hESCs into cortical excitatory neurons using the dual-SMAD inhibition protocol (Shi *et al*, 2012). We examined the effects of IL-17A, *cis*- and *trans*-RSV alone and in combination with IL-17A after 72 hours of treatment at day 55 of differentiation in cortical excitatory neurons (**Fig. 1A-E and Supplementary Fig. S1**). Neurite outgrowth analysis showed a significant decrease in mean and total neurite length with IL-17A and with IL-17A + *trans*-

137 RSV but not with *cis*-RSV (**Fig. 1B-C**). Similarly, neuronal arborization, as assessed by complexity
138 index, was reduced in IL-17A and IL-17A + *trans*-RSV conditions (**Fig. 1D**), while Scholl analysis
139 had a similar non-significant trend for IL-17A alone (**Fig. 1E**). These findings indicate that IL-17A
140 disrupts neuronal morphogenesis, with *trans*-RSV amplifying these effects.
141 Next, we evaluated the effect of IL-17A, *cis*- and *trans*-RSV on neuronal activity using multi-
142 electrode array (MEA) approaches after a 24-hour treatment for day 55 cortical excitatory neurons.
143 Neurons for each treatment were cultured in 8 wells containing electrodes, and spontaneous
144 neuronal activity was measured for 15 minutes every 2 hours for a total of 24 hours. By day 55 of
145 neuronal induction cortical excitatory neurons are becoming synaptically active (**Fig. 1F-G**).
146 Weighted mean firing rates showed a non-significant decrease in IL-17A-treated neurons but a
147 significant reduction in neurons treated with IL-17A + *trans*-RSV (**Fig. 1F**). Spike counts were
148 significantly lower with IL-17A alone and with IL-17A combined with either *cis*-RSV or *trans*-RSV,
149 while no significant effects were observed with RSV isomers alone (**Fig. 1G**). These results suggest
150 that IL-17A reduces neuronal activity, with differential contributions from RSV isomers.
151
152 To dissect the mechanisms underlying these deficits, we examined dynamic microtubules, critical for
153 neurite growth and synaptic plasticity, using tyrosinated tubulin as a marker (Hosseini *et al*, 2022;
154 Moutin *et al*, 2021). Imaging analysis of cellular tyrosinated tubulin after 72 hours showed a
155 reduction in tyrosinated tubulin in neurons treated with *trans*-RSV, IL-17A + *cis*-RSV, and IL-17A +
156 *trans*-RSV, but not in IL-17A alone or *cis*-RSV alone (**Fig. 1H-I**). Western blot analysis after 4 hours
157 of treatment showed a significant decrease in all conditions, with the largest decrease in neurons
158 treated with IL-17A, *trans*-RSV, and combination treatments (**Supplementary Figure S1**). Reduced
159 tyrosinated tubulin levels may reflect altered activity of tyrosine tubulin ligase (TTL), TyrRS, or both.
160 Interestingly, total TTL levels increased in neurons treated with IL-17A, *trans*-RSV, IL-17A + *cis*-RSV
161 and IL-17A + *trans*-RSV, potentially reflecting a compensatory response to preserve microtubule
162 integrity. Total TyrRS levels also trend upward, achieving significance in IL-17A-treated neurons
163 compared to control neurons (**Supplementary Figure S1**). However, imaging analysis after 4 hours
164 of treatment showed reduced TyrRS levels in the nucleus, implying a nuclear depletion of TyrRS by
165 IL-17A (**Supplementary Figure S1**). Together, these results highlight how inflammation and RSV
166 isomers affect pathways regulating microtubule dynamics and neuronal homeostasis. In summary,
167 IL-17A impairs neuronal morphogenesis and activity in human cortical neurons, with *trans*-RSV
168 exacerbating these effects.
169
170 **IL-17A elicits activation of specific downstream signaling pathways in human neurons**

171 The observed changes in tyrosinated tubulin suggest disruptions in microtubule dynamics,
172 potentially driven by signaling pathways such as STAT3 and NF-κB (Jackman *et al*, 2009; Verma *et*
173 *al*, 2009), both implicated in immune downstream signaling. In non-neuronal systems, IL-17A
174 activates different signaling pathways, including NF-κB, JAK/STAT, and MAPK (Rex *et al*, 2023),
175 while in human neuronal progenitor cells (NPCs), IL-17A stimulation leads to the activation of ERK,
176 RPS6, and NF-κB signaling pathways (Gomes *et al*, 2022). To investigate these pathways in
177 differentiated neurons, we examined day 55 cortical excitatory neurons following 4 hours of
178 treatment (**Fig. 2A-F**). Analysis of total cell lysates showed that IL-17A, *trans*-RSV and IL-17A +
179 *trans*-RSV all increased total STAT3 levels, but only IL-17A + *trans*-RSV significantly elevated
180 phospho-STAT3 (p-STAT3) levels (**Fig. 2A-C**). In contrast, phospho-MAPK (p-MAPK) and NF-κB2
181 were significantly upregulated by IL-17A or *trans*-RSV individually, but not in combination (**Fig. 2D-**
182 **E**). However, the total levels of NF-κB were upregulated with both *cis*- and *trans*-RSV as well as IL-
183 17A + *trans*-RSV, while IL-17A alone had no significant effect (**Fig. 2F**). To clarify this discrepancy,
184 we examined the nuclear localization of NF-κB as a marker of its activation. Nuclear NF-κB levels
185 were significantly increased in neurons treated with IL-17A, *trans*-RSV, and IL-17A + *trans*-RSV but
186 remained unchanged with *cis*-RSV treatment (**Fig. 2G-H**). This differential activation pattern
187 suggests that IL-17A and RSV isomers engage distinct regulatory mechanisms influencing NF-κB
188 signaling. Taken together, our biochemical and imaging analysis suggest that inflammatory signals
189 activate key pathways, including STAT3, MAPK, and NF-κB, which may contribute to observed
190 defects in microtubule dynamics.
191
192 **Accumulation of DNA damage as a response to inflammatory signals in human neurons**
193 STAT3 and MAPK activation are well-documented contributors to DNA repair mechanisms in non-
194 neuronal cells (Barry *et al*, 2010; Wood *et al*, 2009). Similarly, NF-κB activation has been linked to
195 the cellular response towards DNA damage (Stilmann *et al*, 2009; Wang *et al*, 2017). However, in
196 neurons, unresolved DNA damage can exacerbate inflammatory signaling by releasing nuclear DNA
197 fragments into the cytoplasm, activating the cGAS-STING pathway (Li & Chen, 2018). Subsequent
198 translocation of cGAS to the nucleus would further prevent DNA repair, amplifying genomic
199 instability (Liu *et al.*, 2018). We found that both *trans*-RSV and IL-17A increased nuclear cGAS
200 levels (**Fig. 3A-B**), consistent with potential cytoplasmic DNA release and heightened immune
201 activation. To directly assess DNA damage, we measured nuclear foci for phospho-histone H2A.X
202 (γ-H2A.X), a marker of double-strand breaks (**Fig. 3C-D**). Neurons treated with IL-17A, *trans*-RSV
203 or their combination showed significantly elevated γ-H2A.X foci, indicating increased accumulation of
204 unrepaired DNA damage.

205

206 Given the observed increase in total TyrRS levels in the IL-17A-treated neurons, we examined its
207 nuclear translocation (**Fig. 2G**), which is known to promote DNA repair under oxidative stress (Wei
208 *et al*, 2014). After a 72-hour treatment, we found nuclear TyrRS levels to be elevated in neurons
209 treated with IL-17A, *cis*-RSV, *trans*-RSV, or IL-17A + *trans*-RSV (**Fig. 3E-F**). This finding suggests
210 that inflammatory treatment may induce oxidative stress, prompting a compensatory response
211 involving TyrRS nuclear localization to mitigate the DNA damage. Together, these findings
212 demonstrate that IL-17A and the *trans*-RSV isomer exacerbate DNA damage and trigger stress
213 response pathways, while *cis*-RSV appears to mitigate some of these effects, suggesting a potential
214 protective role under inflammatory conditions.

215

216 **Pro-inflammatory cytokine IL-17A alters translation, mitochondrial and metabolic pathways in**
217 **human neurons**

218 To explore the molecular mechanisms disrupted by IL-17A in human neurons in relation to *cis*-RSV
219 and *trans*-RSV, we analyzed transcriptomic changes at day 55 following a 24hrs treatment when
220 neurons began to display neuronal activity (**Fig. 4, Supplementary Table S1 and Supplementary**
221 **Fig. S2**). We identified a distinct set of differentially expressed genes (DEGs) in response to IL-17A
222 alone (73 DEGs, FDR<0.1) (**Fig. 4A and Supplementary Fig. S2**). However, treatment with IL-17A
223 + *cis*-RSV (143 DEGs, FDR <0.05) and IL-17A + *trans*-RSV (1044 DEGs, FDR<0.05) showed a
224 more pronounced effect when compared to controls. Specifically, IL-17A + *trans*-RSV led to a
225 significant upregulation of gene expression with 87.8% of DEGs showing significant overexpression
226 (**Fig. 4B-C and Supplementary Fig. S2**). Combination treatments with RSV isomers showed
227 molecular signatures that were distinct from each other (**Fig. 4D and Supplementary Fig. S2**).
228 Functional enrichment analysis showed an overrepresentation of genes involved in translation and
229 mitochondrial function in neurons treated with IL-17A alone. In contrast, neurons treated with either
230 IL-17A + *cis*-RSV or IL-17A + *trans*-RSV showed enrichment in metabolic processes, particularly
231 glycolysis and pyruvate metabolism (**Fig. 4E, Supplementary Fig. S3, and Supplementary Table**
232 **S2**). Additionally, pathways associated with the endoplasmic reticulum (ER) and autophagosome
233 function were enriched in neurons treated with IL-17A + *trans*-RSV (**Fig. 4F, Supplementary Fig.**
234 **S3, and Supplementary Table S3**). Disruption of mitochondrial function, translation, or autophagy
235 have been previously implicated in the pathobiology of ASD, suggesting the mechanistic relevance
236 of our findings in relation to inflammatory pathways affecting neurodevelopment.

237

238 **WGCNA reveals additional regulatory nodes associated with the effect of inflammation on**
239 **human neurons**

240 To gain further insights into the transcriptional influence of IL-17A, *cis*-RSV, and *trans*-RSV at a
241 system level, we performed weighted gene co-expression network analysis (WGCNA) (**Fig. 5,**
242 **Supplementary Fig. S4, and Supplementary Table S4**). WGCNA identified several eigengene
243 networks associated with each treatment, distinct from each other and from the control (**Fig. 5A and**
244 **Supplementary Fig. S4**). We also investigated the correlation between eigengene and single-cell
245 expression and disease association (**Supplementary Fig. S5**). The Allen Brain Atlas single-cell
246 datasets (Tasic *et al*, 2018) showed enrichment of genes expressed in excitatory and inhibitory
247 neurons (green, light cyan, midnight blue and yellow modules), as well as in oligodendrocyte
248 precursors (OPCs) and astrocytes (blue module) (**Fig. 5B**). To examine the potential relationship
249 between dysregulation in neuropsychiatric disorders and alterations in transcriptional profiles driven
250 by inflammation, we used published meta-analysis of neuropsychiatric brain gene expression from
251 the PsychENCODE Consortium (Wang *et al*, 2018). We found that there are modules associated
252 with ASD (blue, pink, and yellow modules), schizophrenia (blue and pink modules), and bipolar
253 disorder (black, pink, red, and yellow modules) (**Fig. 5C**). Next, we conducted functional gene
254 enrichment analysis on the WGCNA datasets to determine whether specific eigengene networks
255 associated with disease phenotypes were enriched in specific functional categories (**Fig. 5D,**
256 **Supplementary Fig. S4 and Supplementary Table S3-S4**). Functional gene enrichment analysis
257 of the WGCNA datasets revealed significant enrichment in eigengene networks associated with
258 translation (royal blue module), autophagy (turquoise module), and RNA processing (blue module).
259 These findings highlight the relevance of inflammatory pathways in modulating gene networks
260 during early brain development, emphasizing their potential impact on neuropsychiatric disease
261 mechanisms.
262
263 **Impact of inflammation on gene expression in ASD: linking translation and immune response**
264 Based on the transcriptional effect of IL-17A as well as *trans*-RSV on human cortical excitatory
265 neurons we observed, we decided to examine the extent to which these transcriptional changes
266 might overlap with molecular signatures associated with ASD patients. Therefore, we selected a
267 group of ASD patients that presented with a larger head circumference and in some instances were
268 exposed to infections postnatally or in utero, hereafter referred to as ASDi (**Supplementary Table**
269 **S5**). To begin to understand the connection between inflammation and ASD pathogenesis in
270 unaffected and ASD subjects, peripheral blood mononuclear cells (PBMCs) were collected and
271 transformed into lymphoblastoid cells and subjected to metabolic profiling and transcriptome
272 analysis. Metabolic profiling was conducted on lymphoblastoid cells using different cytokines (IL-6,
273 IL-1β, IL-8, TNF-α and IFN-γ) that have been previously associated with ASD (**Fig.6A**). Metabolic
274 profiling revealed decreased responsiveness to certain cytokines (IL-6, IL-1β, IL-8, IFN-γ) in ASD

275 lymphoblasts compared to controls, with no significant difference for TNF-α. To explore the potential
276 mechanisms that could underlie the response to the different cytokines we conducted a
277 transcriptome analysis of a subset of the ASDi cohort that in addition to sensitivity to disease also
278 had a larger head circumference (**Supplementary Table S5**). Transcriptome analysis in ASDi
279 lymphoblastoid cells identified distinct gene expression signatures compared to controls, with
280 upregulated DEGs involved in chromosome segregation and cell division and downregulated DEGs
281 related to translation and immune function (**Fig. 6B-C, Supplementary Fig. S5, Supplementary**
282 **Table S6-S7**). Gene ontology analysis highlighted enrichment for pathways controlling translation,
283 cell division, as well as endoplasmic reticulum function (**Fig. 6C and Supplementary Table S7**).
284 Additionally, functional enrichment analysis revealed upregulated RNA binding activity among the
285 DEGs, suggesting a significant role of RNA processing in the response to inflammation (**Fig. 6D**).
286 Similarly, molecular function analysis by EnrichR revealed a major node comprised by upregulated
287 DEGs associated with RNA binding (**Supplementary Fig. S5 and Supplementary Table S7**).
288 Additionally, KEGG pathway analysis identified several viral response pathways, in addition to
289 splicing and translation signatures (**Fig. 6E**). Finally, disease analysis showed enrichment for
290 Schizophrenia and Parkinson's disease among the upregulated DEGs (**Fig. 6F and Supplementary**
291 **Table S6**). Therefore, our transcriptomic studies in human neurons and in ASDi patient
292 lymphoblastoid cells suggest that dysregulation of translation might be a common molecular
293 signature associated in some instances with ASD cases that present with immune dysfunction and
294 potentially with the effect of MIA in the developing brain.
295
296
297 **DISCUSSION**
298 The effects of MIA on the fetal developing brain are increasingly documented across multiple animal
299 models (Vacharasin *et al*, 2024). However, mechanistic understanding of human-specific
300 mechanisms underlying the impact of inflammation on the fetal brain remains limited. The advent of
301 stem cell technology in combination with two- and three-dimensional neural models is now allowing
302 us to dissect the complex immune-neuro axis in order to understand how increased inflammation
303 could affect human fetal brain development (Freitas *et al*, 2018). Our studies using hESC-derived
304 cortical excitatory neurons uncover a novel mechanism linking inflammation to increased DNA
305 damage and the subsequent activation of the cGAS-STING pathway. While the cGAS-STING
306 dysfunction has been previously implicated in neuroimmune and neurodegenerative diseases (Li *et*
307 *al*, 2024), its role in ASD pathogenesis has not been previously reported. Increasing evidence
308 implicates proteins involved in the DNA damage response in multiple neurodevelopmental disorders
309 (Cunningham *et al*, 2024). However, the connection between increased DNA damage with cGAS-

STING activation in response to inflammatory signals and autism pathogenesis in human neurons has not been previously reported. The connection between DNA damage, cGAS-STING activation, and autism pathogenesis in human neurons underscores a critical gap in the current understanding, highlighting the need for more specific human models to study neurodevelopmental disorders. More importantly, our work further suggests that the increased DNA damage could be in part associated with increased oxidative stress, as indicated by increased nuclear translocation of TyrRS in human neurons treated with inflammatory signals. Under oxidative stress, nuclear translocation of TyrRS will suppress protein synthesis and protect against DNA damage (Cao *et al.*, 2017; Jones *et al*, 2023; Wei *et al.*, 2014). This mechanism is crucial because it points to a potential pathway through which oxidative stress could exacerbate DNA damage in neurons, linking it to neurodevelopmental disorders like ASD. The dysregulation of gene programs controlling translation in response to inflammation, observed in both human neurons and ASD patient lymphoblasts, suggests a broader impact on cellular function in response to inflammatory signals, potentially affecting the neuro-immune axis in ASD.

Our work also highlights the importance of mitochondrial function during brain development, as a major transcriptomic signature we observed was altered in human neurons treated with different inflammatory cues. Modulation of Ca+ signaling and ATP production by mitochondria are essential for synapse development and plasticity (Khaliulin *et al*, 2024) and could be underlying the defects in spontaneous neuronal activity we observed in neurons treated with IL-17A and *trans*-RSV. These disruptions may contribute to the defects in spontaneous neuronal activity observed in treated neurons, suggesting that mitochondria play a crucial role in modulating the response to inflammation during development. Additionally, we identified robust metabolic changes in response to inflammatory signals, particularly in glucose metabolism, indicating a metabolic reprogramming akin to what is seen in immune cells (Mouton *et al*, 2023). This suggests that neurons respond to inflammation by altering their metabolic processes, which could influence cellular functions critical for brain development.

In conclusion, our study provides new insights into how inflammation disrupts molecular pathways in human neurons, particularly highlighting the connection between DNA damage, oxidative stress, and immune response. The involvement of the cGAS-STING pathway and mitochondrial dysfunction in response to inflammatory signals offers a deeper understanding of ASD pathogenesis and points to potential therapeutic targets for intervention. By distinguishing the effects of different resveratrol isomers—*cis*-RSV as potentially protective against inflammation—this work emphasizes the need for targeted therapies that can modulate these pathways in developing neurons. Future research will

345 continue to explore these mechanisms in greater detail, particularly as they relate to the
346 development of therapeutic strategies for neurodevelopmental disorders affected by inflammation.
347
348
349 **MATERIALS AND METHODS**
350
351 **Stem cell culture**
352 Human embryonic stem cells (ESC) H9 were obtained from WiCell and were cultured as previously
353 described (Lizarraga *et al*, 2021). ESC colonies were inspected daily to ensure there was no
354 spontaneous differentiation. ESCs were maintained in mTeSR™ Plus basal medium supplemented
355 with 5X supplement (STEMCELL Technologies, #100-0276) seeded on Matrigel (Corning #354277)
356 coated plates. ESCs were fed daily and were passaged every 3-4 days at a 1:6 ratio using
357 ReLeSR™ (STEMCELL Technologies, #100-0483) following manufacturer protocol. To minimize
358 chromosomal abnormalities, ESCs were maintained only up to passage 50.
359
360 **Generation of forebrain cortical excitatory neurons from human ESCs**
361 H9 ESCs were differentiated into forebrain cortical excitatory neurons as described previously
362 (Lizarraga *et al.*, 2021; Shi *et al.*, 2012). Briefly, ESC colonies were dissociated with Gentle Cell
363 Dissociation Reagent (STEMCELL Technologies, #100-0485) and were plated in mTeSR™ Plus
364 medium (STEMCELL Technologies, #100-0276) supplemented with ROCK inhibitor Y27632
365 (STEMCELL Technologies, #72304) at 1x 10^6 cells per well into 12- well tissue culture plates coated
366 with Matrigel (Corning #354277). After twenty four hours, a complete monolayer should have
367 formed and cell media was replaced with neural induction medium (NIM) made with 1:1 DMEM/F-12
368 GlutaMAX (Thermo Fisher Scientific, #10565018) and Neurobasal media (Thermo Fisher Scientific,
369 #21103049) supplemented with: N2 (Thermo Fisher Scientific #17502-048), B27 (Thermo Fisher
370 Scientific, #17504044), 5µg/ml insulin (Sigma-Aldrich, #I0526-5ML), 1mM L-glutamine (Thermo
371 Fisher Scientific, #25-030-081), 100 µM nonessential amino acids (Thermo Fisher Scientific, #11-
372 140-050), 100µM β-mercaptoethanol (Sigma-Aldrich, #M6250-100ML), 50U/ml penicillin-
373 streptomycin (Thermo Fisher Scientific, #15-140-122), 1µM Dorsomorphin (STEMCELL
374 Technologies,#72102) and 10µM SB431542 (STEMCELL Technologies, #72234). Neuronal
375 progenitors were expanded in NIM with the addition of 10µM recombinant FGF2 (PeproTech, #100-
376 18C) from days 17 to 21. After day 21, neurons were fed with half media changes every other day
377 using neural maintenance medium (NMM), containing all the components of NIM except for
378 Dorsomorphin and SB431542. For subsequent experiments neurons were seeded on either 8-well

379 chamber slides or multi-well tissue culture plates coated with 20µg/ml laminin (Sigma-Aldrich,
380 #L2020-1MG) and poly-ornithine (Sigma-Aldrich, #P4957-50ML).
381
382 **Western blotting**
383 For western blot analysis, neurons at day 55 of neuronal induction were washed twice with cold 1X
384 PBS and lysed in cell lysis buffer (20 mM Tris-HCl (pH 7.5), 150 mM NaCl, 1 mM Na_2EDTA, 1 mM
385 EGTA, 1% Triton, 2.5 mM sodium pyrophosphate, 1 mM beta-glycerophosphate, 1 mM Na_3VO_4,
386 1 µg/ml leupeptin supplemented with protease inhibitor). The lysates were centrifuged at 12,000 *g* for
387 15 min at 4 °C. Lysates were quantified using Pierce BCA Protein Assay kit (Thermo Scientific
388 #23227), and equal amounts of protein were loaded onto a 4 to 12% gradient gel (NuPAGE
389 Invitrogen). Protein was transferred from the gel to 0.2 µm NC membranes at 25 V for 10 min using
390 transfer stacks (iBlot3 Invitrogen) and blocked with LiCor TBS blocking buffer (#927-60003) for
391 1 hour at room temperature before application of primary antibodies. Primary and secondary
392 antibodies were incubated overnight at 4 °C and for 1 hour at room temperature, respectively.
393 Membranes were incubated with primary antibodies using the following dilutions: cGAS (Proteintech,
394 #26416-1-AP 1:500), STAT3 (Cell Signaling Technology, #9139S, 1:500), phospho-STAT3 (Cell
395 Signaling Technology, #9145S,1:500), NF-κB (Cell Signaling Technology, #8242S, 1:500), NF-κB2
396 (Cell Signaling Technology, #3017S, 1:500), TyrRS (Abcam, #ab50961, 1:1000), TTL (Proteintech,
397 #66076-1-IG, 1:1000), Tyrosinated tubulin (Millipore Sigma, #MAB1864-I,1:2000), MAPK (Cell
398 Signaling Technology, #9102S, 1:1000), p-MAPK (Cell Signaling Technology, #9101S, 1:1000), and
399 GAPDH (Cell Signaling Technology, #97166S, 1:1000) prepared in LiCor Intercept T20 (TBS)
400 Antibody Diluent (#927-65003). Blots were washed 1X TBST (10 mM Tris-HCl pH 8.0, 150 mM
401 NaCl, 0.01% Tween-20) after primary antibody incubation. Fluorescent secondary antibodies diluted
402 at 1:5000, were used for anti-rabbit (Thermo Scientific, #A32729), anti-mouse (Thermo Scientific,
403 #A32735), and anti-rat (Thermo Scientific, #A11006). Blots imaged using LiCor Odyssey CLX
404 scanner were quantified using ImageJ (Version 1.53c).
405
406 **Pharmacological Treatments**
407 Stock solutions for RSV were prepared at a concentration of 1000x in ethanol and then diluted into
408 cell culture media to achieve the desired final concentration. *cis*-RSV was purchased from Cayman
409 Chemicals (#10004235, ≥ 98% purity), dissolved in ethanol to prepare a stock solution at 100 mM.
410 *trans*-RSV was obtained from Millipore-Sigma (#34092, ≥ 99% purity) and also dissolved in ethanol
411 to make a 100 mM stock solution. IL-17A was purchased as a lyophilized powder from R&D Systems
412 (#317-ILB-050), dissolved in PBS to create a stock solution of 50 µg/ml, and stored at -80°C until

413 required for use. For all experiments, the treatments were done using 50 μM for RSV isomers and
414 50ng/ml for IL-17A.
415
416 **Immunocytochemistry**
417 At day 32 of neuronal induction, ESC-derived human cortical neurons were plated (30,000 cells/well)
418 in 8-well chamber slides (CELLTREAT, #229168) coated with 0.01% poly-L-ornithine and 20μg/ml
419 laminin. For each experiment, three independent neuronal inductions were used. At day 55,
420 neurons were treated with either DMSO, IL-17A, *cis*-Resveratrol (*cis*-RSV), *trans*-Resveratrol (*trans*-
421 RSV), IL-17A + *cis*-RSV or IL-17A + *trans*-RSV and after 4 hours neurons were briefly rinsed with
422 1XPBS (Thermo Scientific, #70011044), fixed with 4% paraformaldehyde (Electron Microscopy
423 Sciences, #15710-S) for 15 minutes (min) at room temperature, washed three times for 5 min each
424 with 1XPBS, permeabilized with 0.25% Triton X-100 (Sigma-Aldrich, #X100-100ML) for 10 min at
425 room temperature, washed three times for 5 min each with room temperature 1X PBS, and blocked
426 with 10% goat serum solution (Thermo Scientific, #50062Z) for one hour at room temperature. After
427 blocking, primary antibodies against either MAP2 (Abcam #36592 1:1250), NF-κB (Cell Signaling
428 Technology, #8242S, 1:400), cGAS (Proteintech, #26416-1-AP, 1:200), Tyrosinated Tubulin
429 (Millipore Sigma, #MAB1864-I, 1:500), TyrRS (Abcam, #ab50961, 1:50) diluted in 2% goat serum
430 and 0.2% Triton X-100 (Lizarraga *et al.*, 2021) were applied to cells and incubated overnight at 4˚C.
431 Following primary antibody treatment, cells were washed three times with 1XPBS for 5 minutes each
432 time, and then incubated for 1 hour at room temperature with secondary antibodies diluted in 1XPBS
433 with 2% goat serum (AlexaFluor-594 anti-mouse Thermo Fisher Scientific #A11032, Alexa Fluor-647
434 anti-rabbit Thermo Fisher Scientific # A-21245, and Alexa Fluor-488 anti-chicken Thermo Fisher
435 Scientific # A32931, all diluted at 1:1000). Cells were washed three times with 1XPBS, and slides
436 were mounted with ProLong Glass Antifade Mountant with DAPI (Thermo Scientific #P36985) under
437 1 mm rectangular coverslips (Fisher Scientific, #12-548-5P).
438
439 **Image acquisition and analysis**
440 *Imaging:* Images were captured using an FV3000 Olympus Confocal Microscope equipped with a
441 60X or a 20X objective lens. Fluorescent images of 30 to 35 random cells were taken for each
442 experimental condition for at least three independent experiments.

443 *Protein levels intensity analysis:* Protein colocalization was assessed for two different fluorophores
444 by generating a maximum intensity z-projection from image stacks. Regions of interest (ROIs) were
445 created around individual cells using the select tool in Fiji ImageJ, and individual masks were
446 generated to exclude external signals. The ROI was duplicated in split color channels—red (NF-κB,

447 TyrRS, cGAS) and blue (DAPI) or cyan (MAP2) across different images. Pixel intensity values were
448 thresholded across all images to ensure consistency in the analyzed areas and to exclude
449 background noise. The software calculated the mean gray value, representing the average pixel
450 intensity within the selected area. These measurements were grouped per independent neuronal
451 induction and were compared for analysis.

452 *γ-H2A.X foci analysis:* Number of foci per cell were measured for each condition with 30 to 35 nuclei
453 analyzed per condition for each experiment. First, the regions of interest (ROIs) around individual
454 cell nuclei were defined using DAPI staining to mark nucleus boundaries. The analyze Particles
455 function in ImageJ was used to measure γ-H2A.X distribution. After thresholding the images to a
456 uniform value across samples, the number of particles per ROI were counted, representing the
457 number of foci per cell. These measurements were grouped per independent neuronal induction and
458 were compared for analysis.
459

460 **Library preparation and sequencing**

461 RNA was extracted using the RNeasy Micro Kit (Qiagen, #74004) following the manufacturer's
462 instructions. For each sample, RNA quality was analyzed using Agilent 2200 Tape Station system.
463 cDNA libraries were prepared with the Collibri™ Stranded RNA Library Prep Kit for Illumina™
464 Systems (Invitrogen, #A38996096). Sequencing was performed using 150-bp reads using paired-
465 end chemistry on an Illumina NovaSeq, to achieve a depth of 100 million reads.
466

467 **RNA-seq data processing and analysis**

468 We assessed the quality of raw sequence data using FastQC (version 0.11.9) and TrimGalore
469 (version 0.6.6). Raw reads were mapped to the Ensembl reference genome 104 (GRCh38) using
470 the transcript-level quantifier Salmon (version 1.5.2) in mapping-based mode. Count matrices were
471 generated from transcript-level quantification files using the tximport package (version 1.30.2). All
472 RNAseq data is publicly available through GEO #. Differentially expressed genes (DEGs) were
473 identified with DESeq2 (version 1.32.0) (Love *et al*, 2014), considering genes with an adjusted p-
474 value < 0.05 and a fold change $\geq |1.5|$ as statistically significant. Pathway enrichment analysis (GO,
475 KEGG, DisGeNET) was performed using the EnrichR (version 3.2) and clusterProfiler (version
476 4.10.1) package in R.
477

478 **Co-expression network analysis.**

479 To identify modules of co-expressed genes in the RNA-seq data, we carried out weighted gene co-
480 expression network analysis (WGCNA v1.69)(Langfelder & Horvath, 2008). A soft-threshold power

481 was automatically calculated to achieve approximate scale-free topology (R^2>0.85). Networks were
482 constructed with *blockwiseConsensusModules* function with biweight midcorrelation (bicor). The
483 modules were then determined using the dynamic tree-cutting algorithm. To ensure robustness of
484 the observed network, we used a permutation approach recalculating the networks 200 times and
485 comparing the observed connectivity per gene with the randomized one. None of the randomized
486 networks showed similar connectivity, providing robustness to the network inference. Module sizes
487 were chosen to detect small modules driven by potential noise on the adjusted data. Deep split of 4
488 was used to more aggressively split the data and create more specific modules. Spearman's rank
489 correlation was used to compute module eigengene – memory oscillatory signature associations.

490 *Functional Enrichment:* The functional annotation of the genes within the modules was performed
491 using GOstats (v2.56.0) using the GO and KEGG databases. Expressed genes (13818) were used
492 as background. A one-sided hypergeometric test was performed to test overrepresentation of
493 functional categories and Benjamini-Hochberg adjusted p-value used for multiple comparisons
494 correction.

495 *Neuropsychiatric genes:* Autism spectrum disorders associated genes used for **Supplementary Fig.**
496 **S5E** were downloaded from SFARI database (Banerjee-Basu & Packer, 2010). Modules and genes
497 differentially expressed in ASD, SCZ, and BD were downloaded from an independent source(Gandal
498 *et al*, 2018). Differentially expressed cell-type markers from single-nuclei RNA-seq of ASD were
499 downloaded from published dataset (Velmeshev *et al*, 2019).

500 *GWAS data and enrichment:* We used genome-wide gene-based association analysis implementing
501 MAGMA (v1.07) (de Leeuw *et al*, 2015). We used the 13818 protein-coding genes from human
502 gencode v38 as background for the gene-based association analysis. Suplementary table # reports
503 MAGMA statistics for each of the GWAS data analyzed. GWAS acronyms were used for the figures
504 (e.g.*, ASD = Autism Spectrum Disorders, BD = Bipolar disorder, SZ = Schizophrenia).* Gene set
505 enrichment was applied to correlated genes. We used a Fisher's exact test in R with the following
506 parameters: alternative = "greater", conf.level = 0.95. We reported Odds Ratios (OR) and Benjamini-
507 Hochberg adjusted P-values (FDR).
508
509 *Transcriptomic data available upon request.*
510
511 **Metabolic profiling (PM-M) of Lymphoblastoid cell lines**
512 A specialized technology called Phenotype Mammalian MicroArray (PM-M) plates was developed by
513 Biolog (Hayward, CA, USA) to identify metabolic signatures of behavioral symptoms in PMS. To
514 obtain a metabolic profile, lymphoblastoid cell lines (LCLs) were established from peripheral blood

515 samples collected by venipuncture, using lymphocyte immortalization via Epstein–Barr virus
516 (Srikanth *et al*, 2021). LCLs were harvested in Sigma RPMI-1640 with 15% fetal bovine serum
517 (FBS) from Atlanta Biological (Flowery Branch, GA, USA), two mM L-Glutamine, 100 U/mL Penicillin,
518 and 100 µg/mL Streptomycin from Sigma-Aldrich (St. Louis, MO, USA).
519
520 The PM-M plates measure the cellular production of NADH (nicotinamide adenine dinucleotide,
521 reduced form) in the presence of different compounds to assess metabolic activity. Microplates are
522 utilized with diverse molecules, acting as energy sources (plates PM-M1 to M4) or as metabolic
523 effectors (plates PM-M5 to M8). A single compound is within each well, and a colorimetric redox dye
524 chemistry monitors the production of NADH per well. The energy sources include carbohydrates,
525 carboxylic acids, ketone bodies, and nucleotides in plate PM-M1, as well as amino acids (both alone
526 and as dipeptides) in plates PM-M2 to M4. The metabolic effectors include ions in PM-M5, along
527 with cytokines, growth factors, and hormones in PM-M6 to M8. PM-M plates were incubated with
528 20,000 lymphoblastoid cells per well in a volume of 50 µL, using the modified Biolog IF-M1 medium.
529 Media for plates PM-M1 to M4 were prepared by adding the following to 100 mL of Biolog IF-M1: 1.1
530 mL of 100× penicillin/streptomycin solution, 0.16 mL of 200 mM Glutamine (final concentration 0.3
531 mM), and 5.3 mL of fetal bovine serum (final concentration 5%). Cells were incubated for 48 h at
532 37°C in 5% CO2. After this first incubation, Biolog Redox Dye Mix MB was added (10 µL/well) and
533 plates were incubated under the same conditions for an additional 24 h, during which time cells
534 metabolize the sole carbon source in the well. As the cells metabolize the carbon source, tetrazolium
535 dye in the media is reduced, producing a purple color according to the amount of NADH generated.
536 During the 24 h of exposure to dye, plates were incubated in the Omnilog system, which measured
537 the optical density of each well every 15 minutes, generating 96 data points. At the end of the 24-h
538 incubation, plates were analyzed utilizing a microplate reader with readings at 590 and 750 nm. The
539 first value (A_{590}) indicated the highest absorbance peak of the redox dye and the second value (A_{750})
540 gave a measure of the background noise. The relative absorbance ($A_{590-750}$) was calculated per well
541 as previously described (Boccuto *et al*, 2013). The relative absorbance for 20 control and ASD cell
542 lines after treatment with different cytokines was analyzed using one-way ANOVA analysis in
543 Graphpad prism software.
544
545 **Multielectrode Array Analysis**
546 Neurons were seeded on Cytoview48 MEA plates (Axion Biosystems, #M768-tMEA-48W) at a
547 density of 100,000 cells per well on day 40-41 of neuronal differentiation. Plates were pre-coated
548 using poly-D-lysine (100µg/ml) and laminin (20µg/ml) for 1 hour each at 37°C following the standard
549 coating protocol. Neurons were plated in neural maintenance medium (NMM) supplemented with

550 laminin (20μg/mL). After 24 hours, the medium was replaced with BrainPhys medium (STEMCELL
551 Technologies, #05790) containing NeuroCult™ SM1 and N2 supplements (STEMCELL
552 Technologies, #05711 and #07152), dibutyryl cyclic-AMP (500μg/ml; STEMCELL Technologies, #
553 100-0244), GDNF (Peprotech, #450-10) and BDNF (Peprotech, 450-02) both 20 ng/ml, and ascorbic
554 acid (200nM, STEMCELL Technologies, # 72132). Neurons were maintained on MEA plates with
555 half-medium changes every third day until the experiment. On day 55 of differentiation, treatments
556 were applied to eight wells per experimental condition. Following treatment, electrophysiological
557 activity was recorded using the MEA Maestro Pro system (Axion Biosystems) under standard neural
558 activity conditions. Recordings were taken every 2 hours for 15 minutes over a 24-hour period.
559 Throughout the experiment, cells were maintained at 37°C in 5% CO_2. Spike counts and mean-
560 weighted firing rates were obtained from compiled statistics files for each recording. The 24-hour
561 experimental results were analyzed collectively for each condition, grouping data across all time
562 points to assess overall trends and differences.
563

564 **ACKNOWLEDGEMENTS**

565 The authors wish to thank: Current members of the Lizarraga laboratory for critical reading of the
566 manuscript and previous members of the Lizarraga laboratory, Dr. Pankaj Ghate and Dr. Janay
567 Vacharasin for their preliminary observations; the families that participated in the clinical studies at
568 Greenwood Genetics Center (GCC); Dr. Roger Stevens and Dr. Richard Steet at GGC for the
569 generous donation of control and patient lymphoblastoid cells for functional studies in the Lizarraga
570 laboratory; Cyndi Skinner and Jessica Coleman at GGC who handled the patient samples and
571 clinical histories; and Dr. Stefano Berto (Medical University of South Carolina) for sharing WGCNA
572 bioinformatics pipelines. The research reported in this publication was supported by the National
573 Institute of Mental Health of the National Institutes of Health under Award Number R01MH127081 to
574 SBL. The content is solely the responsibility of the authors and does not necessarily represent the
575 official views of the National Institutes of Health.
576
577

578 **AUTHORS CONTRIBUTIONS**

579 SBL and MJ conceived the study, oversaw the experimental design and data analysis, and wrote the
580 manuscript. SBL led the funding acquisition. MJ conducted the majority of the experiments and
581 data analysis. CK and AG contributed to the biochemical and imaging analysis. LB conducted the
582 metabolic experiments. BY contributed to the RNAseq analysis. SM provided advice on DNA
583 damage studies. All authors contributed to editing the manuscript.

584 **MAIN FIGURES AND FIGURE LEGENDS**

585

586 **Figure 1**

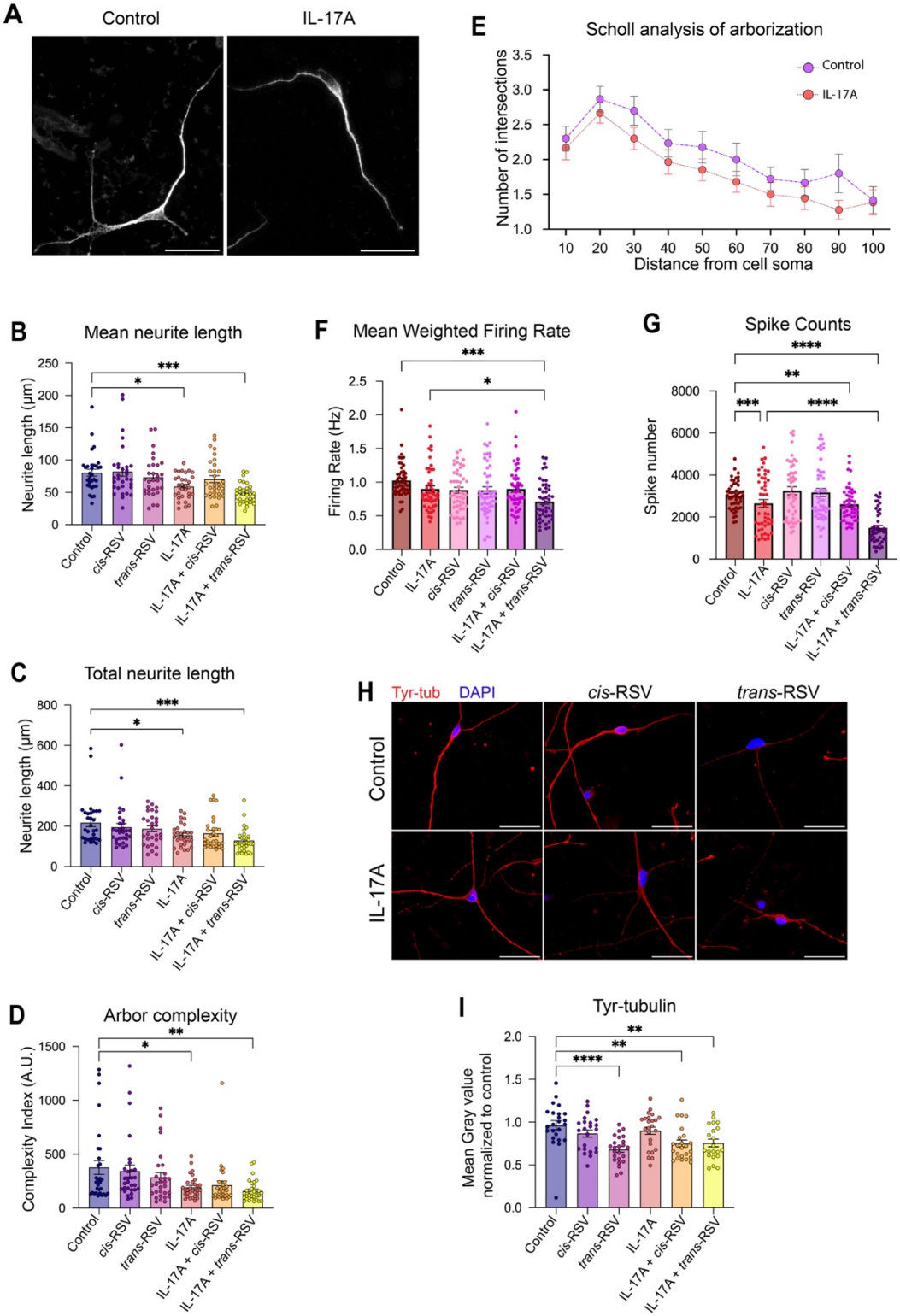

587

588 **Figure 1. Effect of IL-17A, *cis* and *trans*-RSV on neuronal arborization, activity and tubulin**
589 **tyrosination.** (**A**) Representative images show hESC-derived neurons stained with MAP2 in black
590 and white for ease of viewing. Scale bar is 30 µm. (**B-E**) Analysis of neuronal morphogenesis for

control neurons (blue bars and circles), and neurons treated with either *cis*-Resveratrol (*cis*-RSV) (purple bars and circles), *trans*-Resveratrol (*trans*-RSV) (lilac bars and circles), IL-17A (red bars and circles), IL-17A + *cis*-RSV (orange bars and circles), and IL-17A + *trans*-RSV (yellow bars and circles). Mean and standard error of the mean (SEM) are shown for at least 30 neurons measured per condition. (**B**) Graph shows analysis of the mean neurite length; (**C**) Graph shows analysis of total neurite length; and (**D**) Graph shows analysis of arbor complexity by complexity index. Statistical analysis for (B-D) was done using One-way ANOVA with Dunnett's test for multiple comparisons; *P <0.05, **P < 0.005, ***P <0.001. (**E**) Graph shows Scholl analysis for control (purple circles) and IL-17A (red circles) treated neurons. Statistical analysis by mixed model, P values that were not significant are not shown. (**F-G**) Analysis of neuronal activity by weighted mean firing rate (**F**) and spike counts (**G**) for control neurons (brown bar and circles), neurons treated with either IL-17A (red bar and circles), *cis*-RSV (pink bars and circles), *trans*-RSV (light purple bars and circles), IL-17A + *cis*-RSV (magenta bars and circles) and IL-17A + *trans*-RSV (dark purple bars and circles). The average of 3 independent experiments are shown with at least 8 wells per condition. The individual points represent the average per well across 12 different time points and across the 3 independent experiments per condition. Statistical analysis was conducted using grouped analysis by Two-way ANOVA test. *P <0.05, **P < 0.005, ***P <0.001, and ****P < 0.0001. (**H-I**) Analysis of tyrosinated tubulin levels in response to different treatments. (**H**) Representative images are shown stained with a tyrosinated tubulin antibody (red) and nuclei are stained with DAPI (blue). Scale bar is 30µm. (**I**) Quantification of mean gray values for tyrosinated tubulin was analyzed as mean gray value per field for control neurons (blue bars and circles), and neurons treated with either *cis*-RSV (purple bars and circles), *trans*-RSV (lilac bars and circles), IL-17A (red bars and circles), IL-17A + *cis*-RSV (orange bars and circles), and IL-17A + *trans*-RSV (yellow bars and circles). Mean ± SEM are shown with individual points representing individual fields. Statistical analysis was conducted using One-way ANOVA test, **P < 0.005, and ****P < 0.0001.

634 **Figure 2**

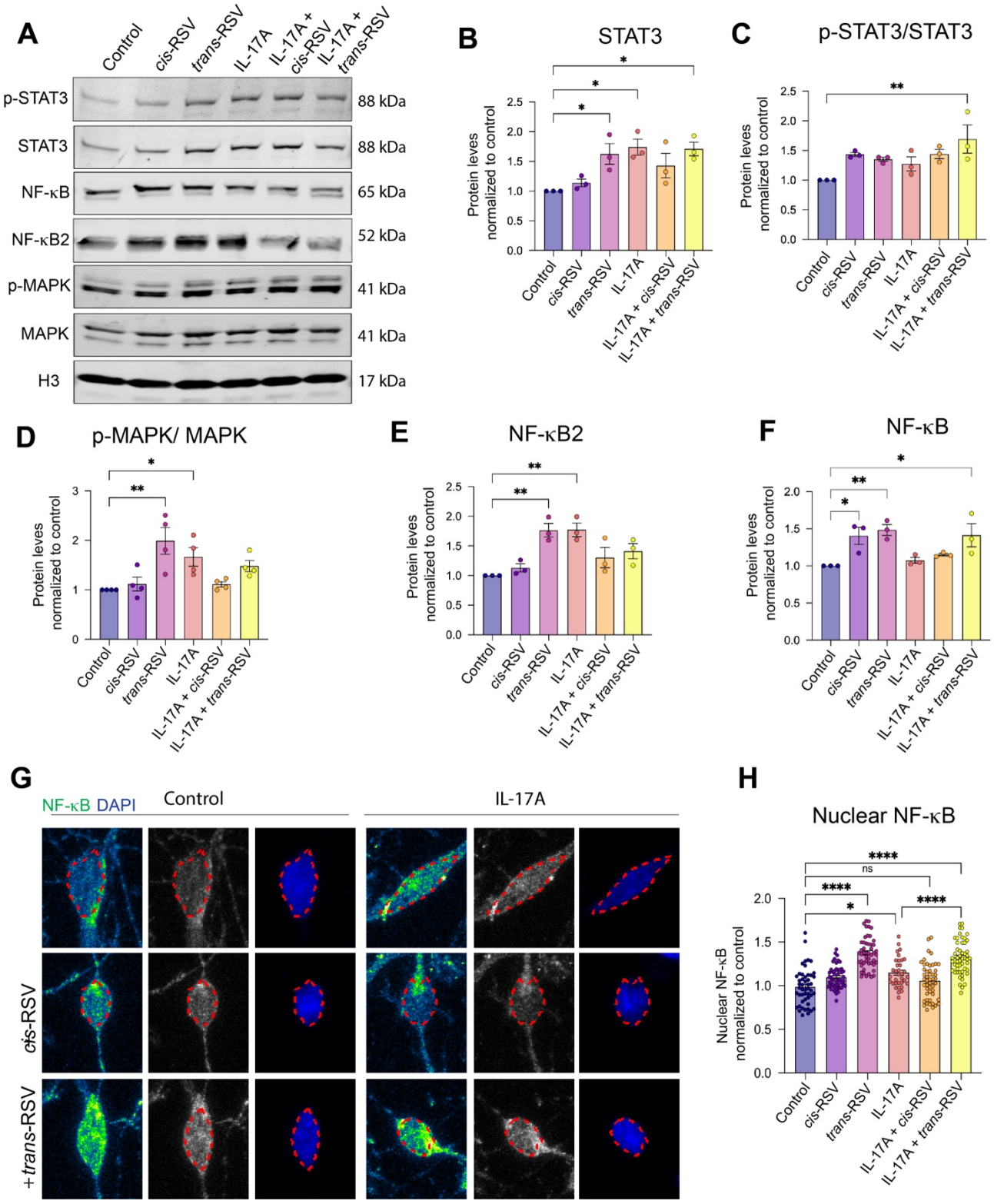

635

636 **Figure 2. Analysis of downstream signaling pathways in human neurons.** (**A**) Representative
637 images show western blot for neuronal cell lysates obtained from either control neurons or neurons
638 treated with IL-17A, *cis*-RSV, *trans*-RSV or IL-17A + *cis*-RSV and IL-17A + *trans*-RSV. Histone H3
639 was used as a loading control for total protein levels unless otherwise specified. Specific protein
640 and their corresponding molecular weights are shown. (**B-F**) Analysis of protein levels for control

neurons (blue bars and circles), and neurons treated with either *cis*-RSV (purple bars and circles), *trans*-RSV (lilac bars and circles), IL-17A (red bars and circles), IL-17A + *cis*-RSV (orange bars and circles), and IL-17A + *trans*-RSV (yellow bars and circles). Mean ± SEM are shown for at least three independent experiments for STAT3 (**B**), phospho-STAT3 (p-STAT3) normalized to STAT3 (**C**), phospho-MAPK normalized to MAPK (**D**), NF-κB2 (**E**) and NF-κB (**F**). Statistical analysis for (**B-F**) was done using ordinary One-way ANOVA; *P <0.05, and **P < 0.005. (**G-H**) Analysis of nuclear translocation of NF-κB in response to different treatments. (**G**) Representative images for neurons stained with an NF-κB antibody shown for which the signal is shown as the LUT (green) and nuclei are stained with DAPI (blue). Scale bar is 10μm. (**H**) Quantification of mean gray values for nuclear NF-κB was analyzed for 30 neurons in 3 independent experiments for control neurons (blue bars and circles), and neurons treated with either *cis*-RSV (purple bars and circles), *trans*-RSV (lilac bars and circles), IL-17A (red bars and circles), IL-17A + *cis*-RSV (orange bars and circles), and IL-17A + *trans*-RSV (yellow bars and circles). Mean ± SEM are shown with individual points representing the average across three independent experiments. Mean gray values were normalized to the control. Statistical analysis was conducted as grouped analysis using two-way ANOVA with Sidak's test, *P < 0.05, and ****P < 0.0001.

692 **Figure 3**

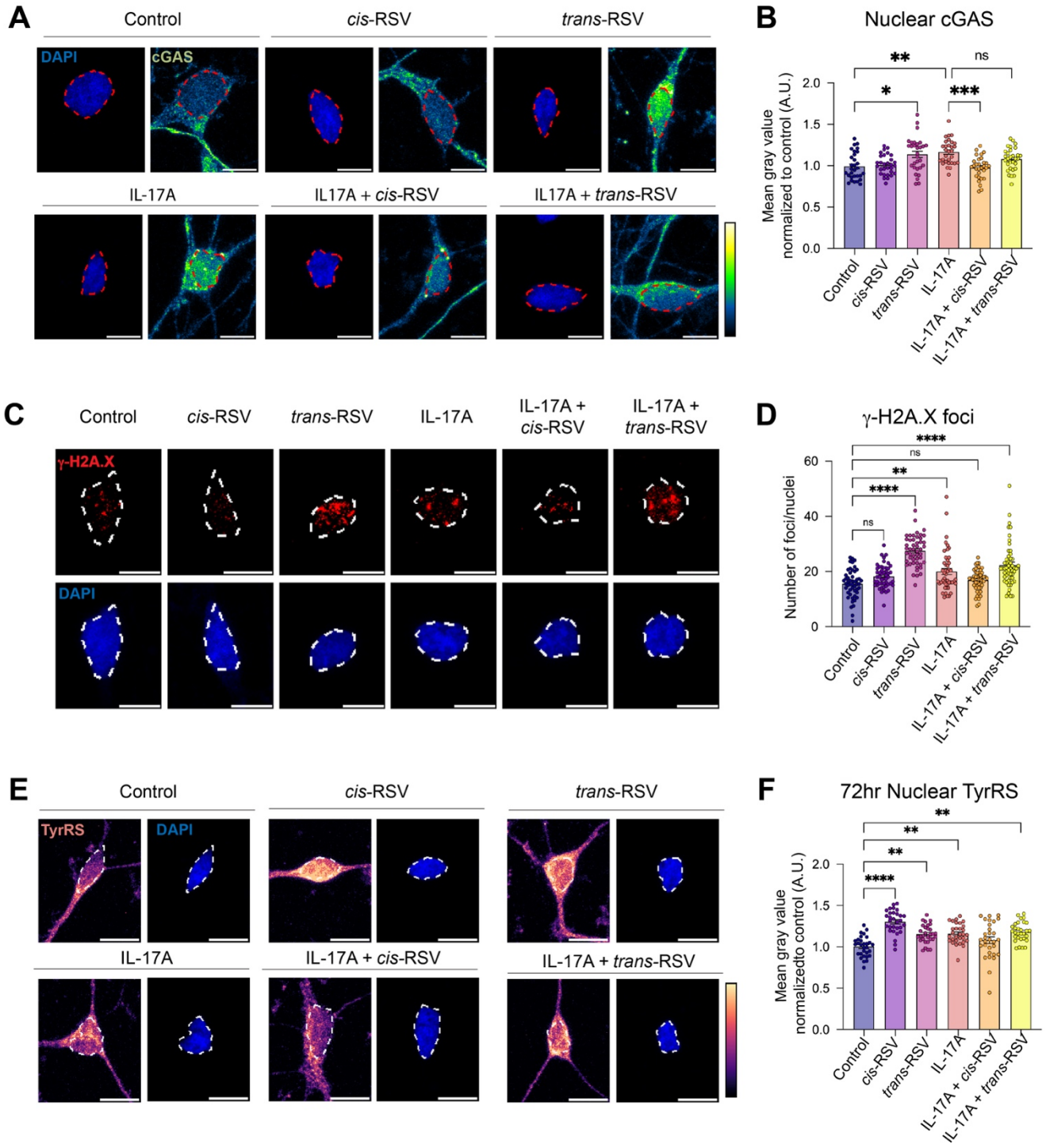

693

694 **Figure 3. Analysis of the effect of inflammation on DNA damage in human neurons.** (**A**)
695 cGAS nuclear translocation in response to different treatments. Representative images of neurons
696 stained with cGAS antibody are shown as the LUT (green) and nuclei are stained with DAPI (blue).
697 Red outline shows the region that was measured. Scale bar is 10μm. (**B**) Quantification of mean
698 gray values for nuclear cGAS was analyzed for 30 neurons in 3 independent experiments for control
699 neurons (blue bars and circles), and neurons treated with either *cis*-Resveratrol (*cis*-RSV) (purple
700 bars and circles), *trans*-Resveratrol (*trans*-RSV) (lilac bars and circles), IL-17A (red bars and
701 circles), IL-17A + *cis*-RSV (orange bars and circles), and IL-17A + *trans*-RSV (yellow bars and
702 circles). Mean ± SEM are shown with individual points representing the average across 30 neurons

in three independent experiments. Mean gray values were normalized to the control. Statistical analysis was conducted as grouped analysis using two-way ANOVA with Sidak's test for multiple comparisons, *P < 0.05, **P < 0.004, and ***P < 0.0009. (**C**) Analysis of γ-H2A.X nuclear foci in response to different treatments. Representative images of neurons stained with γ-H2A.X antibody (red) and nuclei stained with DAPI (blue) are shown. White outline shows the region measured. Scale bar is 10µm. (**D**) Quantification of the number of nuclear γ-H2A.X foci was analyzed for 30 neurons in 3 independent experiments for control neurons (blue bars and circles), and neurons treated with either *cis*-Resveratrol (*cis*-RSV) (purple bars and circles), *trans*-Resveratrol (*trans*-RSV) (lilac bars and circles), IL-17A (red bars and circles), IL-17A + *cis*-RSV (orange bars and circles), and IL-17A + *trans*-RSV (yellow bars and circles). Mean ± SEM are shown with individual points representing the average across 30 neurons in three independent experiments. Statistical analysis was conducted using one-way ANOVA with Sidak's test for multiple comparisons, **P < 0.002 and ***P < 0.00000009. (**E**) TyrRS nuclear translocation in response to different treatments. Representative images of neurons stained with TyrRS antibody are shown as the LUT (pink hues) and nuclei are stained with DAPI (blue). White outline shows the region measured. Scale bar is 10µm. (**F**) Quantification of mean gray values for nuclear TyrRS was analyzed for 30 neurons in 3 independent experiments for control neurons (blue bars and circles), and neurons treated with either *cis*-Resveratrol (*cis*-RSV) (purple bars and circles), *trans*-Resveratrol (*trans*-RSV) (lilac bars and circles), IL-17A (red bars and circles), IL-17A + *cis*-RSV (orange bars and circles), and IL-17A + *trans*-RSV (yellow bars and circles). Mean ± SEM are shown with individual points representing the average across 30 neurons in three independent experiments. Mean gray values were normalized to control. Statistical analysis was conducted as grouped analysis using two-way ANOVA with Sidak's test for multiple comparisons, **P < 0.0099, and ***P < 0.000000005.

754 **Figure 4**

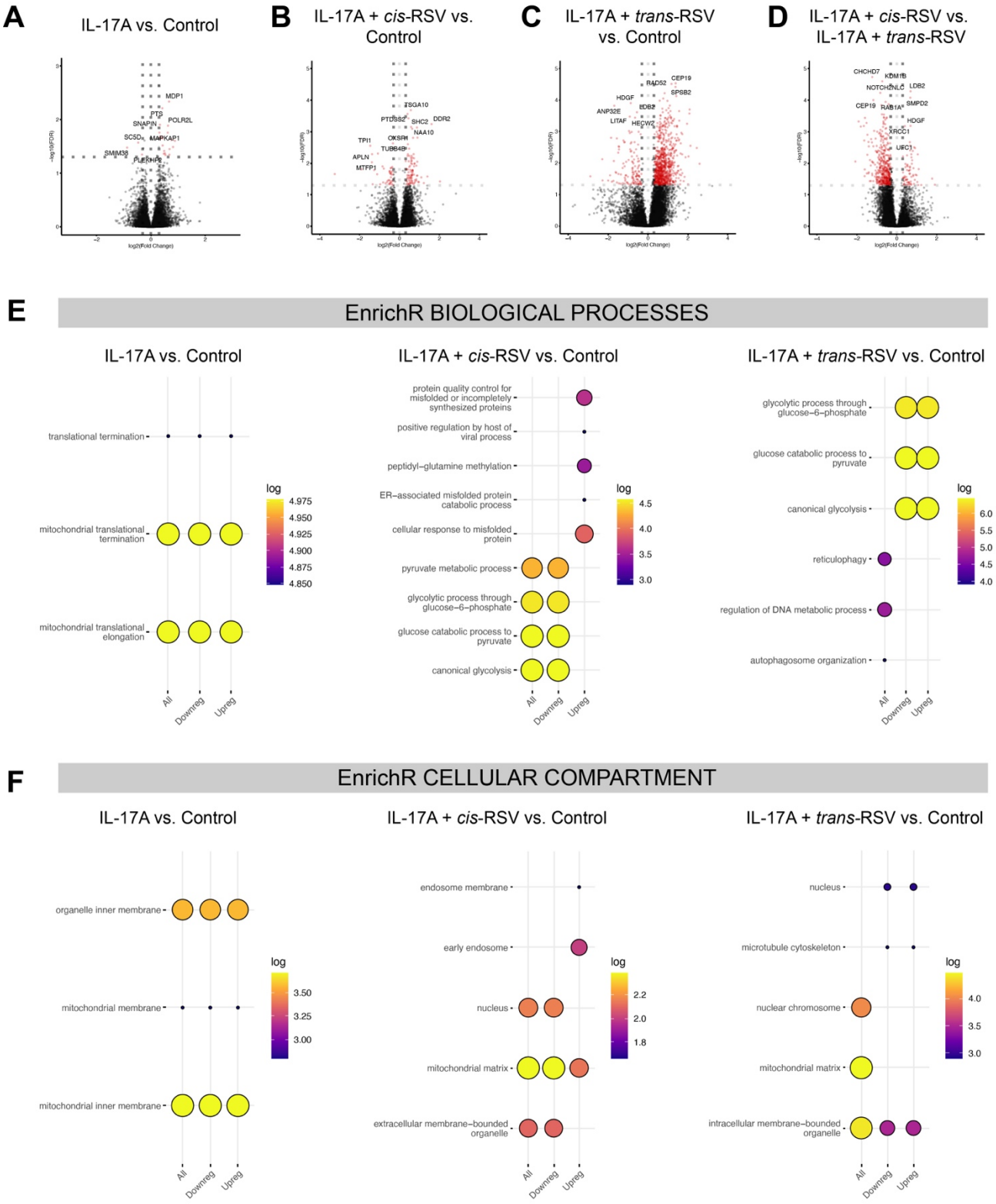

755

756 **Figure 4. IL-17A, *cis*- and *trans*-RSV alter transcriptional programs associated with translation,**
757 **mitochondrial function, and metabolism.** (**A-D**) Volcano plots showing DEGs in human neurons
758 treated with either IL-17A (**A**), IL-17A + *cis*-RSV (**B**) and IL-17A +*trans*-RSV (**C**), compared to control or
759 comparing IL-17A + *cis*-RSV vs. IL-17A + *trans*-RSV (**D**). Log_2 fold changes (LFC) gene expression (x-
760 axis) and $-log_{10}$ adjusted P values (y-axis) generated from DESeq2 differential gene expression analysis
761 are shown. Vertical dotted lines represent 0.58 LFC (1.5 FC) and horizontal dotted line shows adjusted

P=0.05. Significant DEGs are shown in red with the top DEGs labelled in the plot. (**E-F**) Functional enrichment analysis by EnrichR for biological process (**E**), and cellular compartment (**F**), show enrichment for all DEGs, upregulated and downregulated DEGs in IL-17A vs Control neurons or IL-17A + *cis*-RSV vs. control neurons or IL-17A + *trans*-RSV vs. control neurons. Circle size represents the number of DEGs in that category and the color represents the adjusted P value.

814 **Figure 5**

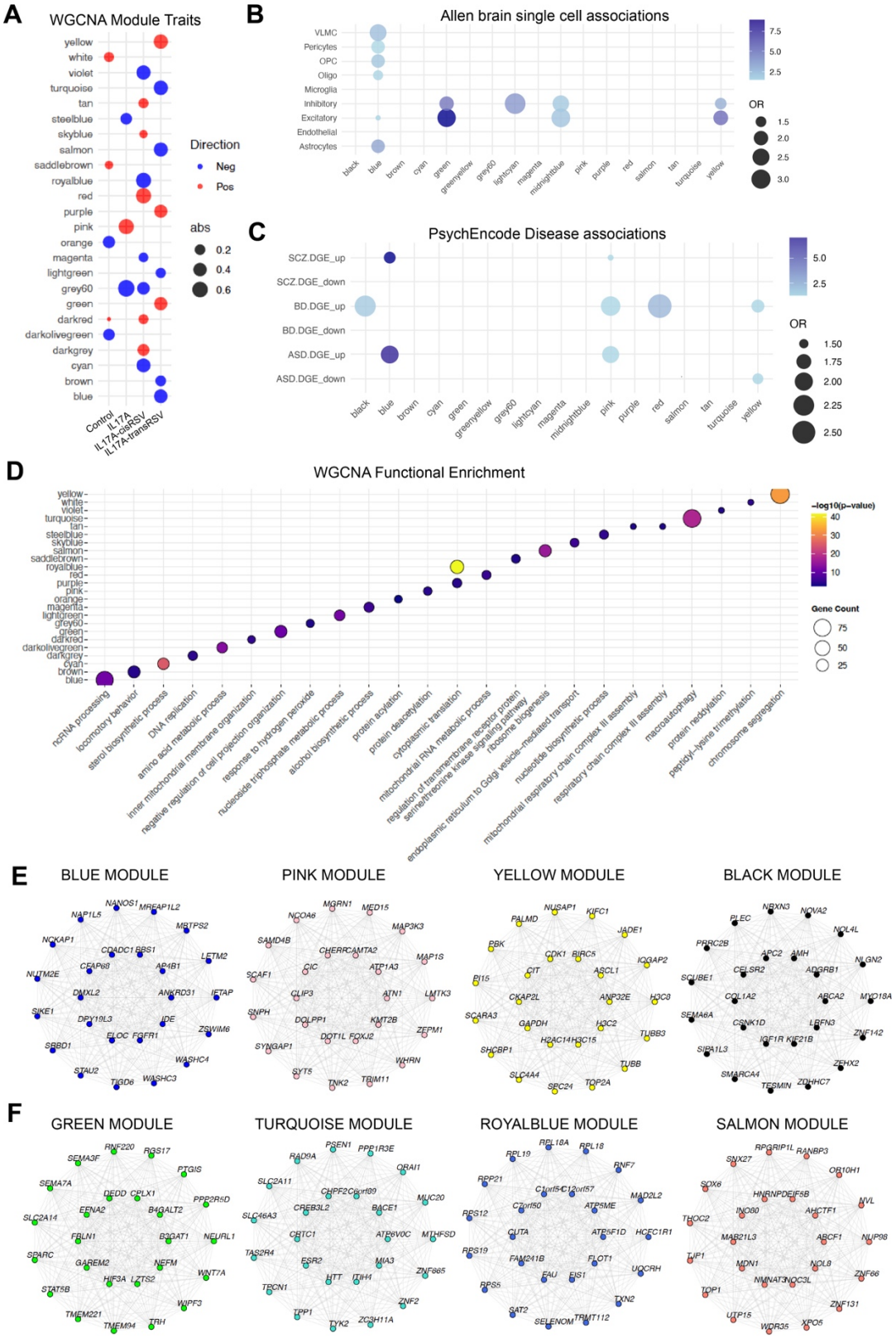

815

816 **Figure 5. Disease association and functional enrichment by WGCNA analysis.** (**A**) WGCNA
817 module trait relationships are shown for control, IL-17A, IL-17A + *cis*-RSV and IL-17A + *trans*-RSV
818 samples. Each module is represented with the direction of gene expression change, indicated as either
819 positive (red) or negative (blue). (**B**) Magma plots show WGCNA enrichment for single cell expression

from the Allen brain atlas. (**C**) WGCNA modules showing disease association with neuropsychiatric disorders highlights upregulated and downregulated DEGs within each module. The size of the solid black circles corresponds to the number of DEGs, and the color intensity of blue represents the log P value, with darker hues indicating greater significance. (**D**) WGCNA pathway enrichment analysis is shown across the different modules with colors depicting the log P value, indicating the significance of the enriched pathways. (**E-F**) Gene networks are shown with relevant hub genes for the blue, pink, yellow, and black modules (**E**), and for the green, turquoise, royalblue, and salmon modules (**F**).

Figure 6

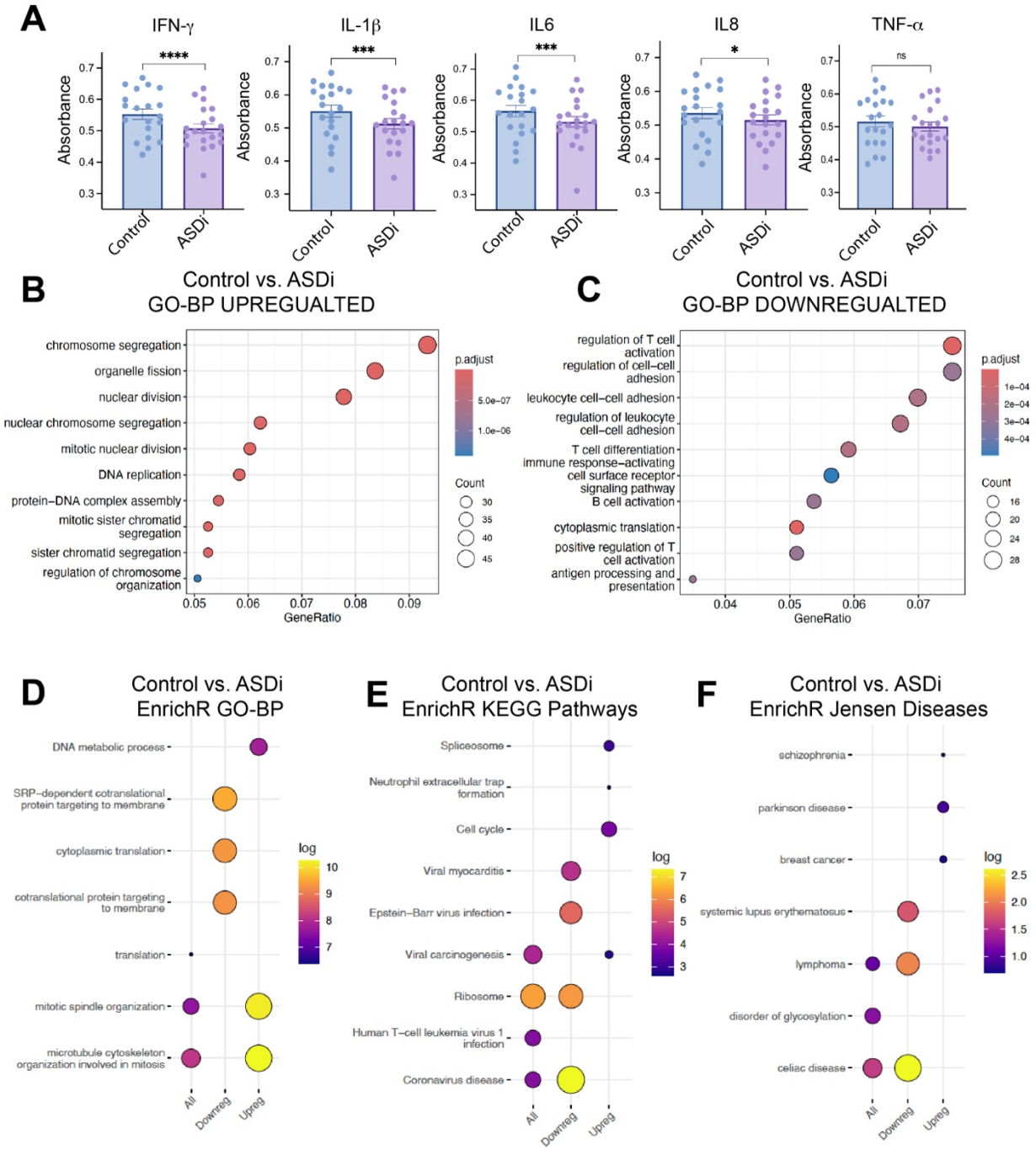

Figure 6. Metabolic and transcriptome analysis of ASD patient lymphocytes. (**A**) Graphs show biolog measurements for control (blue bars and circles) and ASDimmune (ASDi) (purple bars and circles) patient lymphocytes treated with different cytokines. Mean + SEM are shown with individual circles representing the average across multiple measurements. Data was analyzed as grouped data using two-way ANOVA. *P <0.04, ***P < 0.0004, and ****P < $10e^{-15}$. (**B-C**) Gene enrichment analysis using gene ontology (GO) for biological process (BP) for upregulated (**B**) and downregulated DEGs (**C**). (**D-F**) Functional enrichment analysis by EnrichR for biological process (**D**), KEGG pathways (**E**), and Jensen diseases (**F**) show enrichment for all DEGs, upregulated and downregulated DEGs in Control vs. ASDi lymphocytes. Circle size represents the number of DEGs in that category and the color represents the adjusted P value.

885 **REFERENCES**

886 Atladottir HO, Henriksen TB, Schendel DE, Parner ET (2012) Autism after infection, febrile episodes, and antibiotic use during
887 pregnancy: an exploratory study. *Pediatrics* 130: e1447-1454

888 Bakheet SA, Alzahrani MZ, Ansari MA, Nadeem A, Zoheir KM, Attia SM, Al-Ayadhi LY, Ahmad SF (2016) Resveratrol
889 Ameliorates Dysregulation of Th1, Th2, Th17, and T Regulatory Cell-Related Transcription Factor Signaling in a BTBR T + tf/J
890 Mouse Model of Autism. *Mol Neurobiol*

891 Bambini-Junior V, Zanatta G, Della Flora Nunes G, Mueller de Melo G, Michels M, Fontes-Dutra M, Nogueira Freire V, Riesgo
892 R, Gottfried C (2014) Resveratrol prevents social deficits in animal model of autism induced by valproic acid. *Neurosci Lett*
893 583: 176-181

894 Banerjee-Basu S, Packer A (2010) SFARI Gene: an evolving database for the autism research community. *Dis Model Mech* 3:
895 133-135

896 Barry SP, Townsend PA, Knight RA, Scarabelli TM, Latchman DS, Stephanou A (2010) STAT3 modulates the DNA damage
897 response pathway. *Int J Exp Pathol* 91: 506-514

898 Bhandari R, Kuhad A (2017) Resveratrol suppresses neuroinflammation in the experimental paradigm of autism spectrum
899 disorders. *Neurochem Int* 103: 8-23

900 Boccuto L, Chen CF, Pittman AR, Skinner CD, McCartney HJ, Jones K, Bochner BR, Stevenson RE, Schwartz CE (2013)
901 Decreased tryptophan metabolism in patients with autism spectrum disorders. *Mol Autism* 4: 16

902 Cao X, Li C, Xiao S, Tang Y, Huang J, Zhao S, Li X, Li J, Zhang R, Yu W (2017) Acetylation promotes TyrRS nuclear translocation
903 to prevent oxidative damage. *Proc Natl Acad Sci U S A* 114: 687-692

904 Choi GB, Yim YS, Wong H, Kim S, Kim H, Kim SV, Hoeffer CA, Littman DR, Huh JR (2016) The maternal interleukin-17a pathway
905 in mice promotes autism-like phenotypes in offspring. *Science* 351: 933-939

906 Cunningham JL, Frankovich J, Dubin RA, Pedrosa E, Baykara RN, Schlenk NC, Maqbool SB, Dolstra H, Marino J, Edinger J *et al*
907 (2024) Ultrarare Variants in DNA Damage Repair Genes in Pediatric Acute-Onset Neuropsychiatric Syndrome or Acute
908 Behavioral Regression in Neurodevelopmental Disorders. *Dev Neurosci*: 1-20

909 de Leeuw CA, Mooij JM, Heskes T, Posthuma D (2015) MAGMA: generalized gene-set analysis of GWAS data. *PLoS Comput*
910 *Biol* 11: e1004219

911 Eftekharian MM, Ghafouri-Fard S, Noroozi R, Omrani MD, Arsang-Jang S, Ganji M, Gharzi V, Noroozi H, Komaki A, Mazdeh M
912 *et al* (2018) Cytokine profile in autistic patients. *Cytokine* 108: 120-126

913 Fontes-Dutra M, Santos-Terra J, Deckmann I, Brum Schwingel G, Della-Flora Nunes G, Hirsch MM, Bauer-Negrini G, Riesgo RS,
914 Bambini-Junior V, Hedin-Pereira C *et al* (2018) Resveratrol Prevents Cellular and Behavioral Sensory Alterations in the Animal
915 Model of Autism Induced by Valproic Acid. *Front Synaptic Neurosci* 10: 9

916 Freitas BC, Mei A, Mendes APD, Beltrao-Braga PCB, Marchetto MC (2018) Modeling Inflammation in Autism Spectrum
917 Disorders Using Stem Cells. *Front Pediatr* 6: 394

918 Gandal MJ, Zhang P, Hadjimichael E, Walker RL, Chen C, Liu S, Won H, van Bakel H, Varghese M, Wang Y *et al* (2018)
919 Transcriptome-wide isoform-level dysregulation in ASD, schizophrenia, and bipolar disorder. *Science* 362

920 Gomes AKS, Dantas RM, Yokota BY, Silva A, Griesi-Oliveira K, Passos-Bueno MR, Sertie AL (2022) Interleukin-17a Induces
921 Neuronal Differentiation of Induced-Pluripotent Stem Cell-Derived Neural Progenitors From Autistic and Control Subjects.
922 *Front Neurosci* 16: 828646

923 Hosseini S, van Ham M, Erck C, Korte M, Michaelsen-Preusse K (2022) The role of alpha-tubulin tyrosination in controlling the
924 structure and function of hippocampal neurons. *Front Mol Neurosci* 15: 931859

925 Hughes HK, Moreno RJ, Ashwood P (2023) Innate immune dysfunction and neuroinflammation in autism spectrum disorder
926 (ASD). *Brain Behav Immun* 108: 245-254

927 Jackman RW, Rhoads MG, Cornwell E, Kandarian SC (2009) Microtubule-mediated NF-kappaB activation in the TNF-alpha
928 signaling pathway. *Exp Cell Res* 315: 3242-3249

929 Jhanji M, Rao CN, Massey JC, Hope MC, 3rd, Zhou X, Keene CD, Ma T, Wyatt MD, Stewart JA, Sajish M (2022) Cis- and trans-
930 resveratrol have opposite effects on histone serine-ADP-ribosylation and tyrosine induced neurodegeneration. *Nat Commun*
931 13: 3244

932 Jones JA, Wei N, Cui H, Shi Y, Fu G, Rauniyar N, Shapiro R, Morodomi Y, Berenst N, Dumitru CD *et al* (2023) Nuclear
933 translocation of an aminoacyl-tRNA synthetase may mediate a chronic "integrated stress response". *Cell Rep* 42: 112632

934 Khaliulin I, Hamoudi W, Amal H (2024) The multifaceted role of mitochondria in autism spectrum disorder. *Mol Psychiatry*

935 Kimura A, Kishimoto T (2010) IL-6: regulator of Treg/Th17 balance. *Eur J Immunol* 40: 1830-1835

936 Langfelder P, Horvath S (2008) WGCNA: an R package for weighted correlation network analysis. *BMC Bioinformatics* 9: 559

937 Lee BK, Magnusson C, Gardner RM, Blomstrom A, Newschaffer CJ, Burstyn I, Karlsson H, Dalman C (2015) Maternal
938 hospitalization with infection during pregnancy and risk of autism spectrum disorders. *Brain Behav Immun* 44: 100-105

939 Li Q, Wu P, Du Q, Hanif U, Hu H, Li K (2024) cGAS-STING, an important signaling pathway in diseases and their therapy.
940 *MedComm (2020)* 5: e511

941 Li T, Chen ZJ (2018) The cGAS-cGAMP-STING pathway connects DNA damage to inflammation, senescence, and cancer. *J Exp*
942 *Med* 215: 1287-1299

943 Liu H, Zhang H, Wu X, Ma D, Wu J, Wang L, Jiang Y, Fei Y, Zhu C, Tan R *et al* (2018) Nuclear cGAS suppresses DNA repair and
944 promotes tumorigenesis. *Nature* 563: 131-136

945 Lizarraga SB, Ma L, Maguire AM, van Dyck LI, Wu Q, Ouyang Q, Kavanaugh BC, Nagda D, Livi LL, Pescosolido MF *et al* (2021)
946 Human neurons from Christianson syndrome iPSCs reveal mutation-specific responses to rescue strategies. *Sci Transl Med* 13

947 Lombardo MV, Moon HM, Su J, Palmer TD, Courchesne E, Pramparo T (2018) Maternal immune activation dysregulation of
948 the fetal brain transcriptome and relevance to the pathophysiology of autism spectrum disorder. *Mol Psychiatry* 23: 1001-
949 1013

950 Love MI, Huber W, Anders S (2014) Moderated estimation of fold change and dispersion for RNA-seq data with DESeq2.
951 *Genome Biol* 15: 550

952 Lydholm CN, Kohler-Forsberg O, Nordentoft M, Yolken RH, Mortensen PB, Petersen L, Benros ME (2019) Parental Infections
953 Before, During, and After Pregnancy as Risk Factors for Mental Disorders in Childhood and Adolescence: A Nationwide Danish
954 Study. *Biol Psychiatry* 85: 317-325

955 Moutin MJ, Bosc C, Peris L, Andrieux A (2021) Tubulin post-translational modifications control neuronal development and
956 functions. *Dev Neurobiol* 81: 253-272

957 Mouton AJ, Aitken NM, Moak SP, do Carmo JM, da Silva AA, Omoto ACM, Li X, Wang Z, Schrimpe-Rutledge AC, Codreanu SG
958 *et al* (2023) Temporal changes in glucose metabolism reflect polarization in resident and monocyte-derived macrophages
959 after myocardial infarction. *Front Cardiovasc Med* 10: 1136252

960 Rex DAB, Dagamajalu S, Gouda MM, Suchitha GP, Chanderasekaran J, Raju R, Prasad TSK, Bhandary YP (2023) A
961 comprehensive network map of IL-17A signaling pathway. *J Cell Commun Signal* 17: 209-215

962 Sarieva K, Kagermeier T, Khakipoor S, Atay E, Yentur Z, Becker K, Mayer S (2023) Human brain organoid model of maternal
963 immune activation identifies radial glia cells as selectively vulnerable. *Mol Psychiatry* 28: 5077-5089

964 Sciara AN, Beasley B, Crawford JD, Anderson EP, Carrasco T, Zheng S, Ordway GA, Chandley MJ (2020) Neuroinflammatory
965 Gene Expression Alterations in Anterior Cingulate Cortical White and Gray Matter of Males With Autism Spectrum Disorder.
966 *Autism Res* 13: 870-884

967 Shi Y, Kirwan P, Livesey FJ (2012) Directed differentiation of human pluripotent stem cells to cerebral cortex neurons and
968 neural networks. *Nat Protoc* 7: 1836-1846

969 Smith SE, Li J, Garbett K, Mirnics K, Patterson PH (2007) Maternal immune activation alters fetal brain development through
970 interleukin-6. *J Neurosci* 27: 10695-10702

971 Srikanth S, Cascio L, Pauly R, Jones K, Sorrow S, Cubillan R, Chen CF, Skinner CD, Champaigne K, Stevenson RE *et al* (2021) A
972 new test for autism spectrum disorder: Metabolic data from different cell types. *Data Brief* 39: 107598

973 Stilmann M, Hinz M, Arslan SC, Zimmer A, Schreiber V, Scheidereit C (2009) A nuclear poly(ADP-ribose)-dependent
974 signalosome confers DNA damage-induced IkappaB kinase activation. *Mol Cell* 36: 365-378

975 Tasic B, Yao Z, Graybuck LT, Smith KA, Nguyen TN, Bertagnolli D, Goldy J, Garren E, Economo MN, Viswanathan S *et al* (2018)
976 Shared and distinct transcriptomic cell types across neocortical areas. *Nature* 563: 72-78

977 Thomson JA, Itskovitz-Eldor J, Shapiro SS, Waknitz MA, Swiergiel JJ, Marshall VS, Jones JM (1998) Embryonic stem cell lines
978 derived from human blastocysts. *Science* 282: 1145-1147

979 Vacharasin JM, Ward JA, McCord MM, Cox K, Imitola J, Lizarraga SB (2024) Neuroimmune mechanisms in autism etiology -
980 untangling a complex problem using human cellular models. *Oxf Open Neurosci* 3: kvae003

981 Velmeshev D, Schirmer L, Jung D, Haeussler M, Perez Y, Mayer S, Bhaduri A, Goyal N, Rowitch DH, Kriegstein AR (2019) Single-
982 cell genomics identifies cell type-specific molecular changes in autism. *Science* 364: 685-689

983 Verma NK, Dourlat J, Davies AM, Long A, Liu WQ, Garbay C, Kelleher D, Volkov Y (2009) STAT3-stathmin interactions control
984 microtubule dynamics in migrating T-cells. *J Biol Chem* 284: 12349-12362

985 Voineagu I, Wang X, Johnston P, Lowe JK, Tian Y, Horvath S, Mill J, Cantor RM, Blencowe BJ, Geschwind DH (2011)
986 Transcriptomic analysis of autistic brain reveals convergent molecular pathology. *Nature* 474: 380-384

987 Wang D, Liu S, Warrell J, Won H, Shi X, Navarro FCP, Clarke D, Gu M, Emani P, Yang YT *et al* (2018) Comprehensive functional
988 genomic resource and integrative model for the human brain. *Science* 362

989 Wang W, Mani AM, Wu ZH (2017) DNA damage-induced nuclear factor-kappa B activation and its roles in cancer progression.
990 *J Cancer Metastasis Treat* 3: 45-59

991 Wei N, Shi Y, Truong LN, Fisch KM, Xu T, Gardiner E, Fu G, Hsu YO, Kishi S, Su AI *et al* (2014) Oxidative stress diverts tRNA
992 synthetase to nucleus for protection against DNA damage. *Mol Cell* 56: 323-332

993 Wood CD, Thornton TM, Sabio G, Davis RA, Rincon M (2009) Nuclear localization of p38 MAPK in response to DNA damage.
994 *Int J Biol Sci* 5: 428-437

995 Xie W, Ge X, Li L, Yao A, Wang X, Li M, Gong X, Chu Z, Lu Z, Huang X *et al* (2018) Resveratrol ameliorates prenatal progestin
996 exposure-induced autism-like behavior through ERbeta activation. *Mol Autism* 9: 43
997